

Article

Surfactant-Free Synthesis of Reduced Graphene Oxide Supported Well-Defined Polyhedral Pd-Pt Nanocrystals for Oxygen Reduction Reaction

Yongfu Tang ^{1,2,*}, Teng Chen ¹ and Wenfeng Guo ¹

¹ Hebei Key Laboratory of Applied Chemistry, College of Environmental and Chemical Engineering, Yanshan University, Qinhuangdao 066004, China

² Key Laboratory of Preparation and Application of Environmental Friendly Materials (Jilin Normal University), Ministry of Education, Changchun 130103, China

* Correspondence: tangyongfu@ysu.edu.cn

Received: 23 July 2019; Accepted: 2 September 2019; Published: 9 September 2019



Abstract: Well-defined polyhedral Pd-Pt nanocrystals anchored on the reduced graphene oxide (rGO) are successfully synthesized via a facile and efficient surfactant-free solvothermal route. The formation mechanism is carefully illustrated via tuning the surface state of rGO substrate and the Pd/Pt ratio in Pd-Pt nanocrystals. rGO substrates with continuous smooth surface, which can offer continuous 2D larger π electrons, play important roles in the formation of the well-defined polyhedral Pd-Pt nanocrystals. Suitable Pd/Pt ratio, which determines the affinity between the rGO substrate and polyhedral Pd-Pt nanocrystals, is another important factor for the formation of polyhedral Pd-Pt nanocrystals. Due to the well-defined surface of Pd-Pt nanocrystals, rich corners and edges from polyhedral structure, as well as more exposed (111) facets, the low-Pt polyhedral Pd-Pt nanocrystals anchored on rGO, used as electrocatalysts, exhibit high electrocatalytic activity for oxygen reduction reaction with excellent methanol tolerance.

Keywords: Pd-Pt nanocrystals; electrocatalysts; oxygen reduction reaction; reduced graphene oxide; polyhedral nanocrystals

1. Introduction

Pt-alloy nanocrystals or core-shell structure nanoparticles are the state-of-the-art electrocatalysts for oxygen reduction reaction [1–12]. Among them, Pt-Pd nanocrystals with well-defined morphology and structure exhibits excellent performances [6–12]. Surfactants or polymers are usually used as protectors to stabilize the well-defined morphology of the Pd-Pt nanocrystals [6–9], or complicated organic oleic acid/oleylamine synthesis system was applied [12–14]. However, these protectors/organic amines, strongly adsorbing on the active sites and declining the activity of the Pd-Pt electrocatalysts, are hardly removed. Therefore, complicated processes are needed to remove these adsorbed stabilizers or oleic acid/oleylamine solvents, which hinders the large-scale production of the Pd-Pt electrocatalysts and increases their cost. Therefore, developing a facile and efficient surfactant-free synthesis of well-defined polyhedral Pd-Pt nanocrystals in an aqueous system is important for their applications in the electrocatalysis for oxygen reduction reaction.

Due to the high content of exposed atoms in the edges and corners, the surface energy of the well-defined polyhedral Pd-Pt nanocrystals are much higher than the spherical or irregular nanoparticles [8,15–17]. When the size decreased to nanoscale, the elastic tension of the well-defined polyhedral Pd-Pt metal crystals increases sharply due to the increasing surface atoms, edges, and corners. Therefore, the capping agents (also called ‘protecting agents’) including surfactant and polymers were required to reduce the surface energy of the edges and corners or to alter the surface energy order

of different facets in the well-defined polyhedral nanocrystals [15,18–20]. Without these protecting agents, the high surface energy and high elastic tension would drive the metastable well-defined Pd-Pt nano-polyhedrons to transfer into truncated or spherical nanoparticles due to Ostwald's ripening [15,21,22], which makes the template-free synthesis of well-defined Pd-Pt nano-polyhedrons a challenge which is scarcely reported on.

Herein, polyhedral Pd-Pt nanocrystals with well-defined morphology were firstly obtained via a facile and efficient solvothermal process without any surfactant. Ammonia was used as complex agent to control the nucleation and growth process and reduced graphene oxide (rGO) was used as substrate to lower the elastic tension of the well-defined polyhedrons. The rGO, which was obtained by the exfoliation of graphite [23–25], possesses two-dimensional (2-D) conjugated π bond electrons was widely used as the substrate to support other active materials [26,27]. It also acts as the buffer/reservoir to stabilize the high concentration of hanging bonds in the edges and corners of well-defined Pd-Pt polyhedrons [28,29]. Furthermore, the smooth 2-D surface of rGO can anchor the polyhedral nanocrystals by full contact (Scheme S1) to lower the elastic tension of the edges and corners. The effect of the interactions between the polyhedral nanocrystals and the rGO on the morphology of Pd-Pt polyhedral nanocrystals was investigated by tuning the surface groups of rGO and the Pd/Pt ratios in precursors. Due to the rich corners and edges derived from well-defined polyhedral morphology as well as the more exposed (1 1 1) facets, the rGO supported low-Pt polyhedral Pd-Pt nanocrystal electrocatalysts exhibiting high electrocatalytic activity for oxygen reduction reaction and excellent methanol tolerance.

2. Experimental

2.1. Synthesis of Reduced Graphene Oxides Anchored Pd-Pt Nanocrystals

The graphene oxide (GO) was synthesized by exfoliation of graphite oxide which was obtained by modified Hummers methods [30]. To increase the surface functional groups for anchoring the polyhedral Pd-Pt nanocrystals, the GO obtained from the exfoliation of the graphite oxide via Hummers methods was further treated by oxidizing with HCl acidifying KMnO_4 . In brief, 100 mg of GO powder and 500 mg of KMnO_4 were mixed by ultrasonic bath in 100 mL of deionized water for 2 h to obtain a homogeneous dispersion. Then, 10 mL of HCl and 10 mL of H_2O_2 were added drop by drop to remove the residual KMnO_4 and manganese oxides. The treated GO samples, derived from the graphite with 500 mesh size with being further oxidation treated for one time and three times, were denoted as GO500-1 and GO500-3, respectively. In contrast, the GO3500-1 and GO3500-3 samples represent the treated GO samples derived from the graphite with 3500 mesh size with one time and three times acidified treatment, respectively. These treated GO samples were used as substrates to synthesize the rGO anchored polyhedral Pd-Pt nanocrystals with the mass ratio of 4:1 (Pd-Pt metal mass loading of 20 wt %).

In a typical synthesis of polyhedral Pd-Pt nanocrystals, a designed volume of palladium chloride ($2.1405 \text{ mg mL}^{-1}$) and 20 mL ethylene glycol were mixed under magnetic stirring. Subsequently, the color of the solution changed from faint yellow to colorless with the addition of 2 mL ammonia (25 wt %), indicating the formation of $[\text{Pd}(\text{NH}_3)_x]^{2+}$ complex. Then the designed volume of chloroplatinic acid ($3.1768 \text{ mg mL}^{-1}$) was added into the mixture. After being homogeneously mixed, 40 mg of the treated GO samples (homogeneously dispersed in 40 mL ethylene glycol via supersonic dispersion) transferred to the above solution. After stirring for 72 h and ultrasonic treatment for 4 h, the suspension was transferred into a 100 mL Teflon-lined stainless-steel autoclave and was heated at 150°C for 5 h. The samples were collected after washing and freeze-drying. To further investigate the effect of the Pd/Pt ratios in the precursors on the morphology, structure, and electrocatalytic activity of the rGO anchored polyhedral Pd-Pt nanocrystals, three samples with Pd/Pt ratios of 6:1, 3:1, and 1:1—as well as a pure Pt/rGO and a Pd/rGO—denoted as Pd/rGO3500-1, $\text{Pd}_6\text{Pt}_1/\text{rGO3500-1}$, $\text{Pd}_3\text{Pt}_1/\text{rGO3500-1}$, $\text{Pd}_1\text{Pt}_1/\text{rGO3500-1}$, and Pt/rGO3500-1 are obtained via this method.

2.2. Physicochemical Characterizations of the Pd-Pt/rGO Samples

The real Pd/Pt ratios and metal contents in various Pd-Pt/rGO electrocatalysts were measured by AA-6800F/G atomic absorption spectrophotometer (AAS). 10 mg Pd-Pt/rGO electrocatalyst was dissolved in 20 mL aqua regia (mixture of the concentrated HCl and concentrated H₂SO₄). After all the metals were dissolved, the solution was diluted to 50 mL. Then 2 mL of the obtained nickel cobalt nitrate solution was diluted to 50 mL to obtain the solution for the AAS measurement. Powder X-ray diffraction (XRD) patterns of the samples were performed by a Bruker AXS D8 diffractometer with Cu K Radiation ($\lambda = 0.15418$ nm). The morphologies of the Pd-Pt/rGO electrocatalysts were detected by HT 7700 model transmission electron microscopy (TEM, Hitachi Corp., Japan). The defined structure of the samples was measured by high-resolution transmission electron microscopy (HRTEM, JEM-2000, JEOL Corp., Japan). The size distributions of the Pd-Pt nanocrystals of various catalysts were obtained by measuring 200 nanocrystals from bright-field TEM micrographs randomly. The edge of the tetrahedral Pd-Pt nanocrystals was considered as its size, while the longest line between two corners was considered as the size of the octahedral Pd-Pt nanocrystals. The Raman spectrum was measured at 514 nm excitation by a Renishaw apparatus.

2.3. Fabrication of Working Electrode and Electrochemical Measurement

The electrocatalytic activities of rGO anchored polyhedral Pd-Pt nanocrystals were measured by a Princeton Applied Research workstation (Parstat, Potentiostat Galvanostat EIS Analyzer 4000) via typical three-electrode system at a rotate disk electrode (RDE). The working electrode was prepared by follows: 5 mg of the prepared catalyst powder, 2 mg acetylene black, 50 μ L of Nafion (5 wt % solution) and 2 mL isopropyl alcohol were mixed and ultrasonically dispersed for 30 min to form homogeneous suspension. Then, 25 μ L of the suspension was drop-cast on a glassy-carbon (GC) disk electrode ($\Phi = 0.5$ cm) using a microsyringe (25 μ L). The catalyst-coated electrode was dried in air-atmosphere to form a homogeneous thin layer of catalyst. The catalyst loading on the GC electrode is 310 μ g catalysts per square centimeter, corresponding to 62 μ g Pd+Pt metal per square centimeter. The photographs of the bare glass carbon electrode (GC) and the catalyst coated GC (Figure S1) indicate the success of working electrode coverage and the reproducibility of this process. The electrolyte for the measurement is 0.5 M H₂SO₄ solution. Another solution mixed with 0.5 M H₂SO₄ and 0.5 M methanol was used as the electrolyte to evaluate the methanol tolerance of these electrocatalysts. A 1×1 cm² Pt foil and a HgO/Hg electrode were used as the counter electrode and the reference electrode, respectively. The cyclic voltammetry (CV) measurements are performed via potential scanning from 0.10 V to 1.04 V vs.NHE at the rate of 50 mV s⁻¹ and the I-V polarization measurements were performed via negatively potential scanning from 1.14 V to 0.04 V vs NHE at the rate of 5 mV s⁻¹. The rotation rate of the RDE was 1600 rpm (revolution per minute) during the I-V polarization measurement and without rotation during the CV curve measurements. The specific mass activity of the electrocatalyst was evaluated based on the extracted kinetic currents via Equation (1) at the potential of 0.85 V, which is near to the half-wave currents of these electrocatalysts.

$$\frac{1}{j} = \frac{1}{j_k} + \frac{1}{j_d} \quad (1)$$

where the j , j_k , and j_d were the apparent current density, kinetic current density, and limited current density, respectively.

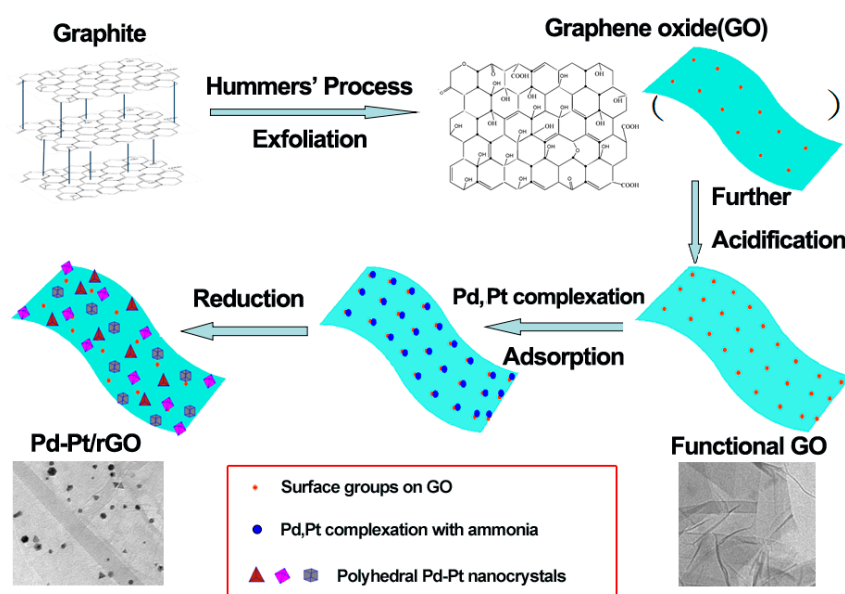
3. Results and Discussion

As shown in Scheme 1, the GO substrates were obtained by exfoliation of graphite oxides, which were prepared by modified Hummers' method [30] using the graphites with size of 500 mesh and 3500 mesh as the pristine materials. After exfoliation of the graphite oxides, the obtained GO was further oxidized by the acidifying treatment which was carefully described in the experimental section.

Figure S2 gives the TEM images of the GO500 and GO3500 substrates, from graphites with 500 mesh and 3500 mesh, respectively. As shown, transparent thin GO nanosheets are observed in both the GO samples. After further oxidation treatment, the GO was dispersed in the solution via ultrasonication. After the further oxidation, the O content was increased from 3.2% to 29.7%, which was carefully characterized in our previous work [31]. Moreover, other characterizations on the graphite, GO, and further oxidized GO had been conducted. The BET and pore size distribution results (Figure S3) indicate that the pores of the GO via further oxidization are 15–25 nm. The Pd and Pt ions, being complexed with ammonia as Equations (2) and (3)



were adsorbed on the GO surface via the plus-to-minus charge adsorption between the Pd/Pt complex and the surface functional groups on GO. During the solvothermal process with ethylene glycol as the solvent and reduction agent, tetrahedral, octahedral, and twinned Pd-Pt seeds are prone to be formed due to the present of the ammonia in the system, which has been discussed in our previous works [11,32,33]. Due to the complexation of the metal ions with ammonia as well as the stabilizing effect of GO substrate, the well-defined polyhedral Pd-Pt nanocrystals are formed via slowly growing from the well-defined polyhedral Pd-Pt seeds. After the GO substrates were further reduced by Na[BH₄] solution to be rGO, uniformly dispersed Pd-Pt nanocrystals on rGO (Pd-Pt/rGO) were finally obtained.



Scheme 1. Scheme for the synthesis of the polyhedral Pd-Pt nanocrystals anchored on the rGO.

At first, the AAS results indicate that the Pd/Pt stoichiometry in all these obtained Pd-Pt based electrocatalysts is near to the designed content. Figure 1 shows the TEM images, XRD pattern and high-resolution TEM (HRTEM) images of the polyhedral Pd₆Pt₁/rGO500-1 with the Pd/Pt ratio of 6:1. As shown in Figure 1a and Figure S4, well-defined tetrahedral, octahedral, and five-fold twinned Pd-Pt nanocrystals are uniformly dispersed on the rGO500-1 substrate. The mean particle size of these nano-polyhedrons is 9 nm with the size scale of 5–20 nm. The peaks in the XRD pattern (Figure 1b), located around 39.9°, 46.3°, 67.9°, 81.6°, and 86.0°, are assigned to the (1 1 1), (2 0 0), (2 2 0), (3 1 1), and (2 2 2) planes of the face-centered cubic (FCC) phase, respectively. These diffraction peaks situated between those of pure FCC Pd(0) (JCPDS 46-1043) and Pt(0) (JCPDS 04-0802). The clear peak splitting, observed in all these peaks, confirms the well-defined morphology and the twinned structures of

the Pd-Pt nanocrystals, which is consistent with the reports [34,35]. The lattice constant of the Pd-Pt nanocrystals was calculated by Bragg's formulation as Equation (4).

$$2d\sin\theta = n\lambda \quad (4)$$

where d , θ , λ , and n are the lattice distance, diffraction angle, wavelength of X-ray, and diffraction order, respectively. The calculated lattice constant of Pd-Pt nanocrystals in the Pd₆Pt₁/rGO500-1 sample is 0.3940 nm, which is markedly higher than that of the theoretic value (0.3894 nm) based on the Vegard's law [17]. This deviation, as well as the peak splitting mentioned above, should be ascribed to the elastic stress from the edges and corners of the well-defined polyhedral nanocrystals. The HRTEM images of the polyhedral nanocrystals in the Pd₆Pt₁/rGO500-1 sample confirm the well-defined morphology. As shown in Figure 1c–e, clear edges and corners are observed in the well-defined tetrahedron, octahedron and five-fold twinned nanocrystals from the Pd₆Pt₁/rGO500-1 sample. The lattice distance observed in these nano-polyhedrons is about 0.228 nm, corresponding to the lattice distance of the expanded (1 1 1) facet, which is in good agreement with the XRD pattern. This result indicates that the polyhedral nanocrystals prefer to expose (1 1 1) facet, which is the highest active facet among the low index facets for oxygen reduction reaction [8,9,21]. The fast Fourier transform (FFT) plots (insets of Figure 1c–e) confirm the exposure of (1 1 1) facet in these polyhedral nanocrystals. It is noted that the lattice distance of the outermost two (1 1 1) facets (0.230 nm), corresponding to the negative split (1 1 1) peak in XRD pattern, is slightly higher than that of inner (1 1 1) facets (0.228 nm), also confirming the lattice expansion derived from the elastic stress of the well-defined polyhedrons.

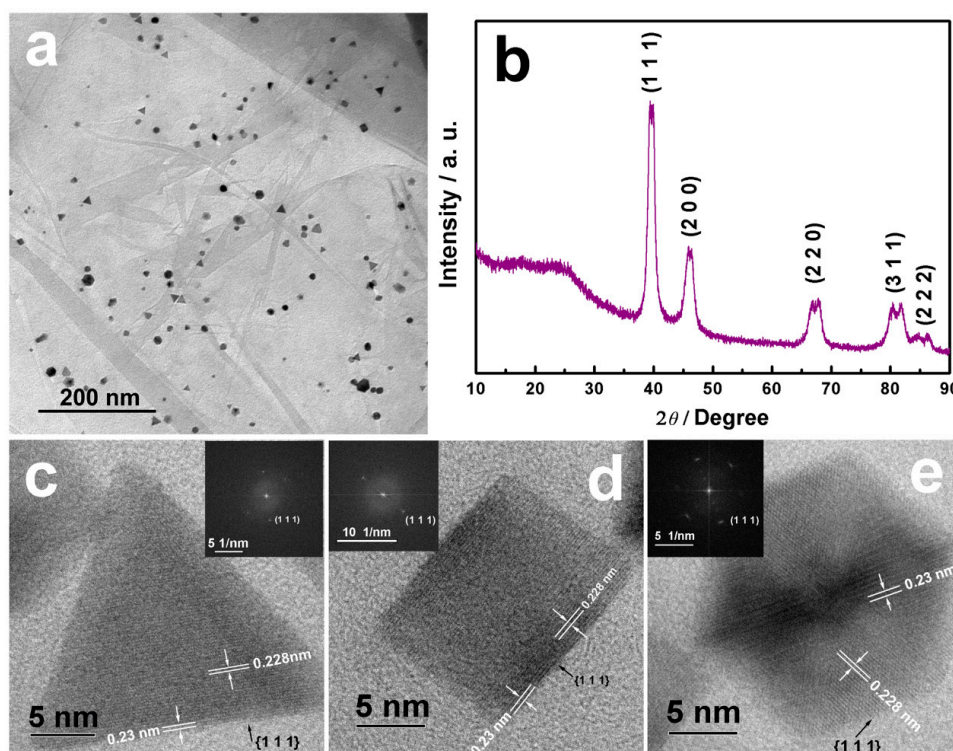


Figure 1. (a) TEM image, (b) XRD pattern, and (c–e) high resolution TEM images (including FFT plots) of the different nanoparticles in Pd₆Pt₁/rGO500-1 sample (c, tetrahedron; d, octahedron; e, five-fold twinned nanocrystal).

To investigate the effect of the surface state of rGO substrate on the formation of the well-defined Pd-Pt nanocrystals, Pd₆Pt₁ nanocrystals anchored on different rGO substrates are synthesized for comparison. The rGO500-1, rGO500-3, rGO3500-1, and rGO3500-3 substrates are derived from the reduction of the GO500 with oxidization treatment for one time (GO500-1) and three time (GO500-3),

and the GO3500 with oxidization treatment for one time (GO3500-1) and three times (GO3500-3), respectively. As shown in Figure 2 and Figure S5, the morphologies of the Pd₆Pt₁ nanocrystals anchored on the rGO500-1 and rGO3500-1 (Figure 1a,b) are more well-defined than those on the rGO500-3 and rGO3500-3 (Figure 2a,c), respectively. Mainly truncated tetrahedrons, irregular octahedrons, and irregular five-fold twinned nanocrystals are observed in the Pd₆Pt₁/rGO500-3 and Pd₆Pt₁/rGO500-3 samples. This should be attributed to the fact that the excessive oxidation (three-time oxidization treatment) can destroy the continuity of the conjugated π bond of the rGO, which is important for the stabilization of the edges and corners in the well-defined polyhedrons. As shown in Figure 2a,c, clear pores observed in the rGO500-3 and rGO3500-3 confirm the incontinuity of the rGO substrate, corresponding to the destroyed 2-D conjugated π bond. Based on the electron buffer/reservoir effect of the 2-D conjugated π bond electrons mentioned in Scheme 1, the destroyed rGO substrates (rGO500-3 and rGO3500-3) possess smaller ability to stabilize the sharp edges and corners, which results in the truncated and irregular morphologies.

The more well-defined morphology of Pd-Pt nanocrystals on the rGO substrates with lower oxidation (rGO500-1 and rGO 3500-1) than those on the rGO substrates with higher oxidation (rGO500-3 and rGO3500-3) are also confirmed by the XRD patterns (Figure 2d). In comparison to the XRD patterns of the Pd₆Pt₁/rGO500-3 and the Pd₆Pt₁/rGO3500-3 samples, the peaks in the XRD patterns of the Pd₆Pt₁/rGO500-1 and the Pd₆Pt₁/rGO3500-1 exhibit a clear negative shift and peak splits (marked with arrows), corresponding to the lattice expansion of the nanocrystals derived from well-defined morphology. The lattice constants of the various Pd₆Pt₁/rGO samples, calculated via Bragg's formula (Equation (4)), are shown in Table S1. The highest lattice constant of Pd₆Pt₁/rGO3500-1 sample should be attributed to its most well-defined morphology and smallest size, both of which can cause high elastic tension from the more exposed atoms in the edges and corners. The crystallite sizes of the Pd-Pt nanocrystals in the obtained catalysts were calculated via Scherrer's equation as $D = K\lambda/(B\cos\theta)$, where D , K , B , λ , and θ are crystallite size, diffraction constant, peak width at half height, wavelength of X-ray, and diffraction angle, respectively. The calculated crystallite sizes of the Pd-Pt nanocrystals in the Pd₆Pt₁/rGO500-1, Pd₆Pt₁/rGO500-3, Pd₆Pt₁/rGO3500-1, and Pd₆Pt₁/rGO3500-3 samples are 6.8, 10.5, 2.1, and 8.6 nm, respectively (Table S1). The smallest crystallite size of the well-defined polyhedral Pd-Pt nanocrystals in Pd₆Pt₁/rGO3500-1 sample confirms the fact that the rGO3500-1 substrate with smooth surface (with fewer defects and surface functional groups) and small size (3500 mesh vs. 500 mesh for rGO500-1) is more suitable for the anchoring of small nanocrystals. Moreover, the sizes of Pd-Pt nanocrystals with well-defined morphology in the Pd₆Pt₁/rGO500-1 and Pd₆Pt₁/rGO3500-1 samples are markedly smaller than their mean particle sizes via the count of nanocrystal sizes in TEM images, which is ascribed to that the polyhedral nanocrystals (specially the 5-fold twinned nanocrystal) consist of more than one crystallite, being demonstrated in our previous works [32,33]. The Raman spectra of the Pd₆Pt₁/rGO500-1, Pd₁Pt₁/rGO500-1, and Pd₆Pt₁/rGO3500-1 (Figure S6) are similar to those of the GO500-1 and GO3500-1 substrates (Figure S7), indicating the synthesis of Pd-Pt nanocrystals and the reduction of GO play a small effect in the crystalline structure of graphene sheets.

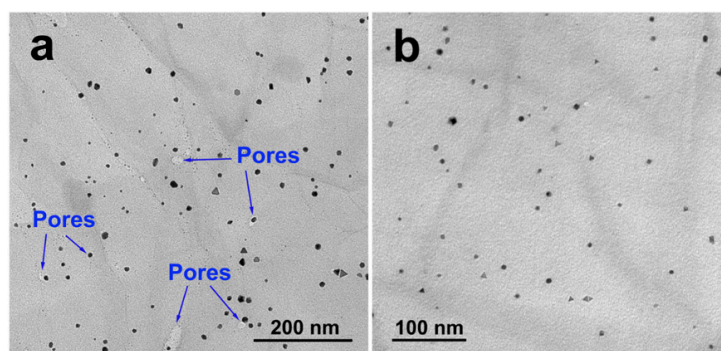


Figure 2. Cont.

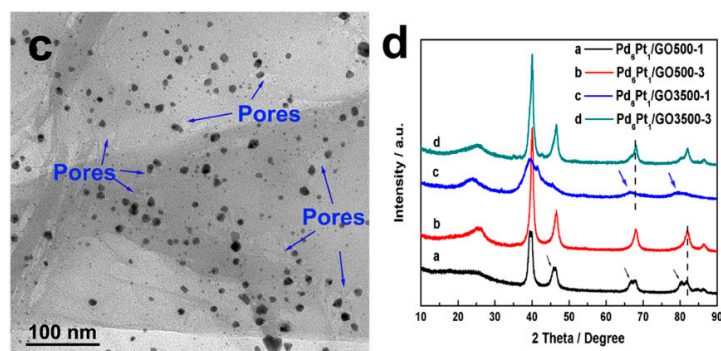


Figure 2. TEM images of the (a) Pd₆Pt₁/rGO500-3; (b) Pd₆Pt₁/rGO3500-1; and (c) Pd₆Pt₁/rGO3500-1 electrocatalysts; (d) XRD patterns of the Pd₆Pt₁/rGO500-1, Pd₆Pt₁/rGO500-3, Pd₆Pt₁/rGO3500-1, and Pd₆Pt₁/rGO3500-3 electrocatalysts.

The shape distributions and size distributions of polyhedral Pd₆Pt₁ nanocrystals on the rGO500-1 and rGO500-3 substrates are given in Figure 3 to illustrate the effect of the surface state of rGO substrate on the morphology of Pd-Pt nanocrystals. As shown in Figure 3a, tetrahedrons, even with the largest elastic tension due to its highest surface atom ratio [15], occupy the largest ratio (53.3%) when the rGO500-1 was used as substrate. In contrast, irregular nanocrystals take up the largest proportion (56.9%) when the rGO500-3 was used as substrate (Figure 3b). Based on the Gibbs-Wulff's crystal growth theory, the well-defined polyhedral Pd-Pt nanocrystals with high surface energy must be stabilized by some covered agent to lower the surface energy. Here the rGO with large 2-D conjugated π bond plays the part of the buffer/reservoir to reduce the surface energy of polyhedral Pd-Pt nanocrystals. Therefore, more well-defined Pd-Pt polyhedrons are obtained on the rGO500-1 with continuous smooth surface (Figure 1a), corresponding to continuous 2-D conjugated π bond. In contrast, due to the richer surface functional groups on the surface of rGO500-3 substrate from the high oxidation extent, the mean particle size of the Pd-Pt nanocrystals on the rGO500-3 (Pd₆Pt₁/rGO500-3, 8.9 nm, Table S1) substrate is smaller than that on the rGO500-1 substrate (Pd₆Pt₁/rGO500-3, 11.9 nm, Table S1). Moreover, the Pd-Pt nanocrystals in Pd₆Pt₁/rGO500-3 sample exhibit more uniform size distribution (Figure 3d) than that in Pd₆Pt₁/rGO500-1 sample (Figure 3c). The smaller particle size and more uniform size distribution should be attributed to the more anchoring sites (surface functional groups) in rGO500-3 to form more Pd-Pt seeds.

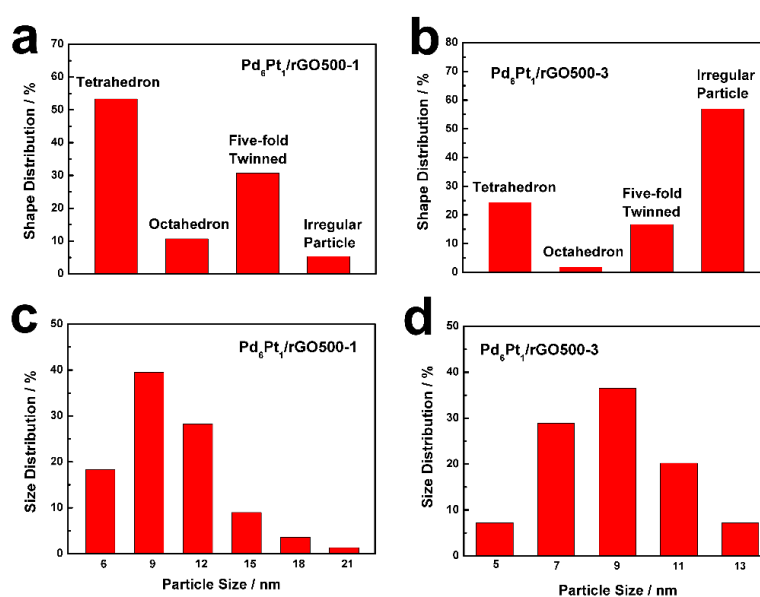


Figure 3. Shape distributions (a,b) and size distributions (c,d) of polyhedral Pd₆Pt₁ nanocrystals on Pd₆Pt₁/rGO500-1 (a,c) and Pd₆Pt₁/rGO500-3 (b,d) substrates.

The comparison of the Raman spectra of rGO500-1, rGO500-3, rGO3500-1, and rGO3500-3 substrates (Figure S7) confirms the higher continuity of large 2-D conjugated π bond in rGO500-1 and rGO3500-1 than that in rGO500-3 and rGO3500-3. As shown, the peaks at 1354 cm^{-1} and 1594 cm^{-1} are assigned to the D band and the G band, respectively. After further acidification, the ratio of D and G band intensities (I_D/I_G) in both rGO500-3 ($I_D/I_G = 1.03$) and rGO3500-3 ($I_D/I_G = 1.04$) are higher than that in rGO500-1 ($I_D/I_G = 0.98$) and rGO3500-1 ($I_D/I_G = 0.74$), respectively, indicating more defects and poor continuity of their surface.

Moreover, the Pd/Pt ratio also plays important roles in the morphology of Pd-Pt nanocrystals due to the different affinities between the metal (Pd, Pt) and the carbon materials, which have been reported in literatures [33,36]. Figure 4 shows the TEM images of the Pd/rGO3500-1, Pd₃Pt₁/rGO3500-1, Pd₁Pt₁/rGO3500-1 and Pd₁Pt₁/rGO3500-1 for comparison with that of Pd₆Pt₁/rGO3500-1 mentioned above. As shown, all the nanocrystals are uniformly dispersed on the surface of rGO substrates, indicating that the anchoring of metal nanocrystals on the rGO is an efficient method to synthesize the highly dispersed Pd-Pt nanocrystals. By the comparison of the Pd-Pt nanocrystals with various Pd/Pt ratios (including pure Pd and Pt) on the rGO substrate, the Pd₆Pt₁/rGO3500-1 shows the most regular well-defined morphology, which is in good agreement with our previous work [11]. The mean particle size distributions of these rGO anchored Pd-Pt nanocrystals are given in Figure S8 and the mean particle sizes are collected in Table S1. With the addition of the platinum, the mean particle sizes of Pd-Pt nanocrystals (6.8 nm in Pd₆Pt₁/rGO3500-1, 8.0 nm in Pd₃Pt₁/rGO3500-1 and 8.8 nm in Pd₁Pt₁/rGO3500-1) are markedly smaller than pure Pd nanocrystals (17.9 nm in Pd/rGO3500-1). The Pt nanocrystals exhibit the smallest size (3.9 nm in Pt/rGO3500-1). This should be attributed to the better affinity between Pt and rGO substrate than that between Pd and rGO substrate. The better affinity, corresponding to the better contact between nanocrystals and rGO substrate, protects the Pd-Pt nanocrystals from aggregating to form larger ones.

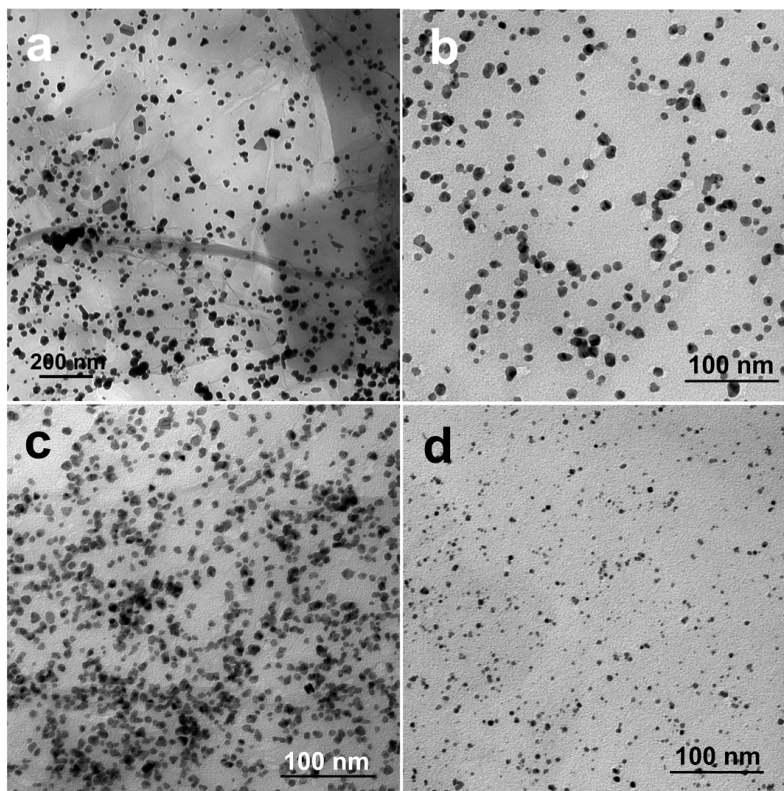


Figure 4. TEM images of the (a) Pd/rGO3500-1; (b) Pd₃Pt₁/rGO3500-1; (c) Pd₁Pt₁/rGO3500-1; and (d) Pt/rGO3500-1 samples.

Figure 5a shows the XRD patterns of the Pd/rGO3500-1, Pt/rGO3500-1, and Pd-Pt/rGO3500-1 samples with different Pd/Pt ratios. The peaks of these samples, located around 39.9° , 46.3° , 67.9° , 81.6° , and 86.0° , are attributed to the (1 1 1), (2 0 0), (2 2 0), (3 1 1), and (2 2 2) facets of the metal faced center cubic phase, respectively. All of them situated between the diffraction peaks of FCC Pd(0) (JCPDS 46-1043) and Pt(0) (JCPDS 04-0802). As shown, positive shifts of the peaks are observed with the increase of Pt content in the Pd-Pt nanocrystals, which deviates from the Vegard's law for the alloys. Figure 5b shows the actual lattice constants of the different samples based on the XRD patterns and the theoretic lattice constants based on Vegard's law. Positive deviations (lattice expansions) are observed in all these samples except Pt/rGO3500-1. The Pd₆Pt₁/rGO3500-1 sample exhibits the highest deviation (1.64%), corresponding to the largest lattice expansion, which should be attributed to the most well-defined morphology and smallest crystallite size. This result demonstrates that the lattice expansion is derived from the elastic stress of the edges and corners in the well-defined tetrahedral, octahedral, and five-fold twinned nanocrystals. The Pd/Pt ratios also play important roles in the crystallite size of polyhedral Pd-Pt nanocrystals due to the different affinities between the different metal (Pd and Pt) and the rGO substrate. As shown in Table S1, the grain sizes of the nanocrystals in Pd/rGO3500-1, Pd₆Pt₁/rGO3500-1, Pd₃Pt₁/rGO3500-1, Pd₁Pt₁/rGO3500-1, and Pt/rGO3500-1, calculated via Scherrer's formula, are 10.3, 2.1, 7.4, 7.0, and 5.1 nm, respectively. The Pd₆Pt₁/rGO3500-1 sample shows the smallest crystallite size.

The reasons for that the best well-defined morphology and smallest crystallite size were obtained with the suitable Pd/Pt ratio of 6/1 in Pd₆Pt₁/rGO3500-1 sample should be attributed to those as follows. As mentioned above, the complexation of Pd and Pt ions via ammonia to control the reduction rate (Equations (2) and (3)), the adsorption of ammonia on the high energy edges/corners to reduce the surface energy [15], as well as the affinity between the rGO substrate and the metal nanocrystals play important roles in the well-defined morphology of polyhedral Pd-Pt nanocrystals. Due to the better affinity between the Pt metal and the rGO substrate than that between the Pd metal and the rGO substrate [33,34], the contact between the Pd-Pt nanocrystals and rGO substrate will become better with the addition of the Pt metal to maintain the well-defined Pd-Pt nanocrystal morphology. On the other hand, the stronger complexation between the Pd ions and ammonia than that between the Pt ions and ammonia causes the faster reduction rate of Pt complexation than that of Pd complexation [32,33]. With the further increasing of the Pt content in the precursor, it will become more difficult to control the growth of the Pd-Pt nanocrystals, which caused the worse well-defined morphology of Pd-Pt nanocrystals with the further increasing of Pt content. Due to the opposite effects of the Pd/Pt ratios on the morphology of polyhedral Pd-Pt nanocrystals, the Pd₆Pt₁ nanocrystals in the Pd₆Pt₁/rGO3500-1 with suitable Pd/Pt ratio exhibit most well-defined morphology.

Due to the well-defined morphology of Pd-Pt nanocrystals with rich edges and corners, as well as the high exposure of active (1 1 1) facets, the Pd-Pt/rGO3500-1 electrocatalysts exhibit high catalytic activity for oxygen reduction reaction (ORR). Due to the high performance of proton exchange membrane with commercial products as Nafion[®] membrane, proton exchange membrane fuel cells are considered the most promising low temperature fuel cells. Therefore, the catalytic activity for ORR in acid electrolyte is more important than that in alkaline electrolyte. Figure 6a shows the CV curves of the Pd/rGO3500-1, Pt/rGO3500-1, and Pd-Pt/rGO3500-1 with different Pd/Pt ratios in 0.5M H₂SO₄ electrolyte. To avoid the hydrogen absorption to Pd bulk in the vicinity of 0.00 V_{vs RHE} [37–42] and the irreversible reconstruction in the course of oxygen adsorption region [43], the potential range of the CV curves were conducted at 0.10~1.04 V_{vs RHE}. As shown, the sharp anodic peaks around 0.05 V ascribed to the reported β -phase absorbed hydrogen [38–41] are absent. The broad peak around 0.20~0.80 V_{vs RHE} is ascribed to the oxidation and recombination of the α -phase and α - β phase transition absorbed hydrogen as well as the adsorbed hydrogen on the surface of Pd-Pt nanocrystals [38–41,43]. The integrated area of the hydrogen absorption/adsorption peaks around 0.20~0.80 V_{vs RHE} with double layer correction (Figure S9a) is corresponding to the qualitative electrochemical active surface area (ECSA) of the Pd-Pt based electrocatalysts. The CV curves of pure rGO with high integrated

area confirms the electric double layer of active materials, which was corrected in the qualitative ECSA. Therefore, the largest hydrogen adsorption peak, the largest metal reduction peak, and the largest electric double layer current in the CV curve of Pd₆Pt₁/rGO3500-1 demonstrate its largest ECSA, which is derived from its smallest crystallite size and most well-defined morphology (more corners and edges). Figure 6b shows the ORR curves of the Pd-Pt/rGO3500-1 with different Pd/Pt ratios, Pt/rGO3500-1 and the commercial JM Pt/C. As shown, when the rGO was used as substrate, the Pt/rGO3500-1 electrocatalyst exhibits slightly higher ORR activity than the commercial JM Pt/C. These Pd-Pt/rGO3500-1 electrocatalysts with low Pt contents exhibit comparable catalytic activity for ORR to that of JM Pt/C catalyst. The specific mass activities based on the total metal mass and based on the Pt mass, which was calculated via extracted kinetic current density as Equation (1), are shown in Figure 6c. The specific mass activity for ORR of the Pt/rGO3500-1 based on the total metal is higher than that of the commercial JM Pt/C, implying that the rGO substrate can improve the catalytic activity of Pt catalyst. The specific mass activity of Pd₆Pt₁/rGO3500-1 based on Pt mass is much higher than those of Pt/rGO3500-1 and JM Pt/C, while both the Pd₃Pt₁/rGO3500-1 and Pd₁Pt₁/rGO3500-1 exhibit lower specific mass activity than Pt/rGO3500-1. The activity based on Pt mass exhibits an order of Pd₆Pt₁/rGO3500-1 > Pt/rGO3500-1 > JM Pt/C > Pd₃Pt₁/rGO3500-1 > Pd₁Pt₁/rGO3500-1. This result indicates that the well-defined morphology and small crystallite size endow the Pd₆Pt₁ nanocrystals in more active Pd₆Pt₁/rGO3500-1 sites—including exposed (1 1 1) facets, corners, and edges—contributing its higher specific mass activity.

Due to the high content of Pd metal which is inert for methanol oxidation, the Pd-Pt/rGO3500-1 electrocatalysts exhibit high methanol tolerance. As shown in Figure 6d. The anodic peaks caused by methanol oxidation, which are clearly in the ORR curves of JM Pt/C and Pt/rGO3500-1, are absent in all the ORR curves of Pd-Pt/rGO3500-1 electrocatalysts. The overpotentials of the Pd₆Pt₁/rGO3500-1, Pd₃Pt₁/rGO3500-1, Pd₁Pt₁/rGO3500-1, Pt/rGO3500-1, and JM Pt/C electrocatalysts, caused by methanol oxidation at 1.0 mA cm⁻², are 3.1, 2.9, 45.6, 45.9, and 271.3 mV, respectively. These results indicate the high methanol tolerance of Pd-Pt/rGO3500-1 electrocatalysts and their potential application in direct methanol fuel cells. The high methanol tolerance of the Pd-Pt/rGO3500-1 electrocatalysts is also confirmed by their low catalytic activities for methanol oxidation reaction (MOR). As shown in Figure S9b–f, clear MOR peaks are observed in the CV curves of JM Pt/C (22.5 mA cm⁻² of peak current, Figure S9b). In contrast, the CV curves of all the Pd-Pt/rGO3500-1 electrocatalysts (Figure S9c–f) are only with slightly higher area in the H₂SO₄ solution with (black solid line) methanol than that without methanol (red dashed line), indicating the inert status of the Pd-Pt/rGO3500-1 electrocatalysts for the MOR, corresponding to their high methanol tolerance.

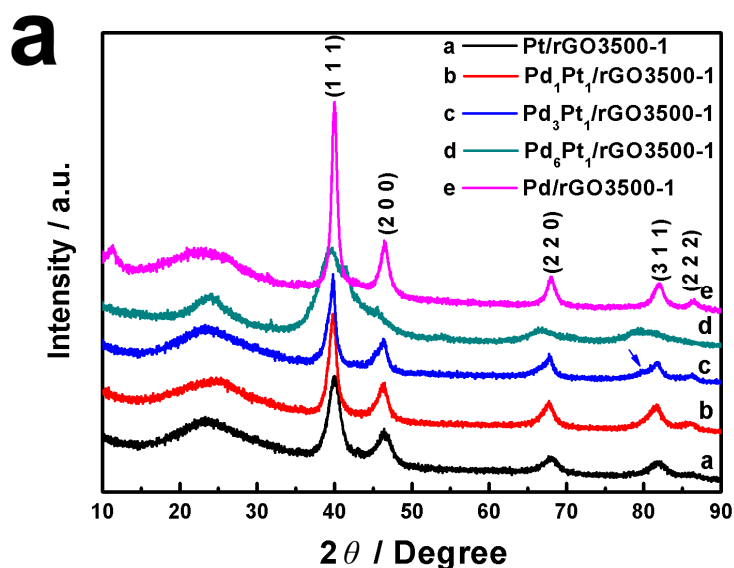


Figure 5. Cont.

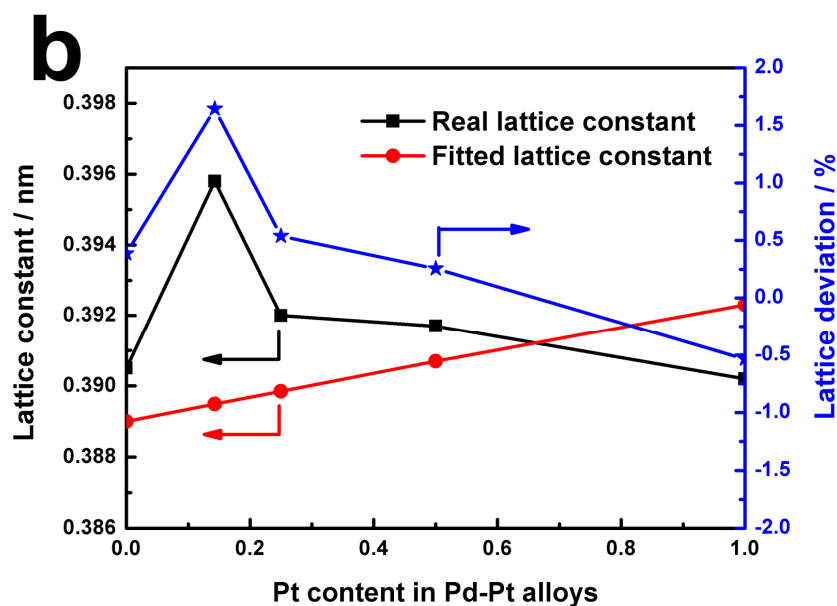


Figure 5. (a) XRD patterns of the Pd/rGO3500-1, Pd-Pt/rGO3500-1 with different Pd/Pt ratios and Pt/rGO3500-1 samples; (b) actual lattice constant and fitted lattice constant based on Vegard's law, as well as the deviation between the actual and fitted data.

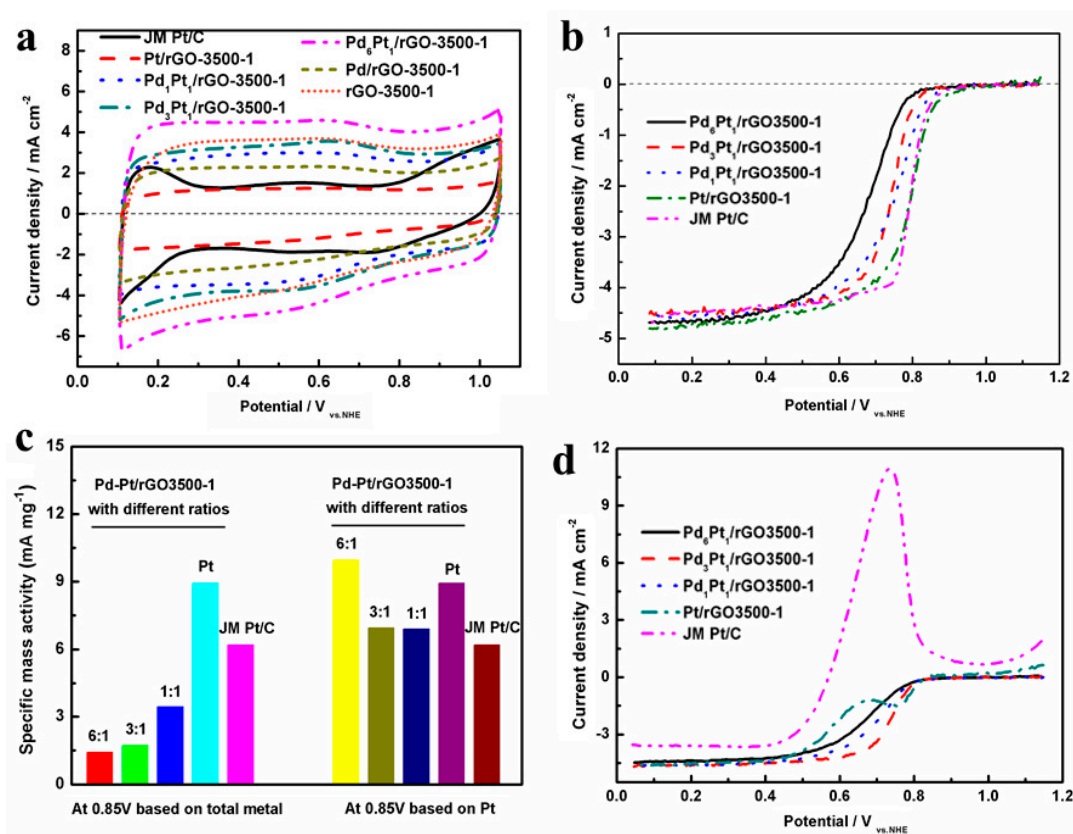


Figure 6. (a) C-V curves and (b) current-potential (I-V) polarization curves of the Pd₆Pt₁/rGO3500-1, Pd₃Pt₁/rGO3500-1, Pd₁Pt₁/rGO3500-1, Pt/rGO3500-1, and JM Pt/C electrocatalysts in the 0.5 M H₂SO₄ solution, scan rate for C-V curves and I-V curves: 50 mV s⁻¹ and 5 mV s⁻¹, respectively. (c) Specific mass activities of different electrocatalysts based on total metal (Pd+Pt, bars at left) and Pt metal (bars at right). The mass loading on the GC electrode for total electrocatalysts and for Pd+Pt metal are 310 and 62 μg cm⁻², respectively. (d) I-V curves of the different electrocatalysts in the 0.5 M H₂SO₄ solution with 0.5 M methanol with the potential scan rate of 5 mV s⁻¹.

4. Conclusions

Well-defined polyhedral Pd-Pt nanocrystals anchored on the rGO substrates were firstly synthesized via a facile and effective surfactant-free process. The formation mechanism of the well-defined polyhedral Pd-Pt nanocrystals was carefully illustrated via tuning the surface state of the rGO substrate and the Pd/Pt ratios in precursors. The various morphologies of the polyhedral Pd-Pt nanocrystals on rGO substrates with different surface states demonstrate that the electrons delocalized from the large π bond of rGO play important roles in stabilizing the hanging bonds of the corners and edges of polyhedral Pd-Pt nanocrystals in the surfactant-free synthesis system. The effect of Pd/Pt ratios on the morphology of polyhedral Pd-Pt nanocrystals indicates that the suitable affinity between the Pd-Pt nanocrystals and rGO substrate is a key factor to obtain well-defined polyhedral Pd-Pt nanocrystals. Lattice expansion and exposed (1 1 1) facets are clearly observed in the well-defined polyhedral Pd-Pt nanocrystals in Pd₆Pt₁/rGO3500-1 sample. Due to the rich edges and corners, as well as the high exposure of active (1 1 1) facets, the Pd-Pt/rGO3500-1 electrocatalysts with low Pt content exhibit high catalytic activity for ORR and good methanol tolerance.

Supplementary Materials: The following are available online at <http://www.mdpi.com/2073-4344/9/9/756/s1>, Scheme S1: The effect of the surface contact between the nanocrystals and the substrate on the elastic tension of the edges and corners Figure S1: Photographs of the bare glass carbon electrode (GC) and the catalysts coated GC, Figure S2: TEM images of the GO500-1 and GO3500-1 substrates, Figure S3: N₂ adsorption-desorption isotherms and pore size distribution of the rGO500-3 substrate, Figure S4: Magnification TEM image of Pd₆Pt₁/rGO500-1 electrocatalyst, Figure S5: Magnification TEM images of the Pd₆Pt₁/rGO500-3, Pd₆Pt₁/rGO3500-1 and Pd₆Pt₁/rGO3500-3 electrocatalysts, Figure S6: Raman spectra of the Pd₆Pt₁/rGO500-1, Pd₁Pt₁/rGO500-1 and Pd₆Pt₁/rGO3500-1 electrocatalysts, Figure S7: Raman spectrum of different GO samples derived from different graphite samples, Figure S8: Particle size distributions and mean particle size of Pd/rGO3500-1, Pd₆Pt₁/rGO3500-1, Pd₃Pt₁/rGO3500-1, Pd₁Pt₁/rGO3500-1 and Pt/rGO3500-1, Figure S9: Double layer corrected calculation for qualitative ECSA, CV curves of the JM Pt/C, Pt/rGO3500-1, Pd₁Pt₁/rGO3500-1, Pd₃Pt₁/rGO3500-1 and Pd₆Pt₁/rGO3500-1 electrocatalysts in the 0.5 M H₂SO₄ solution without and with 0.5 M CH₃OH, Table S1: Lattice constant of rGO anchored Pd, Pt and Pd-Pt nanocrystals obtained with various rGO substrates and different Pd/Pt ratios.

Author Contributions: Y.T. conceived and designed the project. T.C. and W.G. conducted the experimental. Y.T. and W.G. supervised the experimental. Y.T. and T.C. co-wrote the paper. All the authors discussed the results and commented on the manuscript.

Funding: This work was funded by National Natural Science Foundation of China (grant no. 21406191), Specialized Research Fund for the Doctoral Program of Higher Education (grant no. 20131333120011), China Postdoctoral Science Foundation (grant no. 2012M520597), Hundred Excellent Innovative Talents Support Program in Hebei Province (grant no. SLRC2017057), Youth Independent Project of Yanshan University (grant no. 13LGA015), and the Open Project Program of Key Laboratory of Preparation and Application of Environmentally Friendly Materials (Jilin Normal University), Ministry of Education, China (grant no. 2017009). The APC was funded by National Natural Science Foundation of China (grant no. 21406191).

Conflicts of Interest: The authors declare no conflict of interest.

References

1. Wang, L.; Gao, W.; Liu, Z.; Zeng, Z.; Liu, Y.; Giroux, M.; Chi, M.; Wang, G.; Greeley, J.; Pan, X.; et al. Core-shell Nanostructured Cobalt-Platinum Electrocatalysts with Enhanced Durability. *ACS Catal.* **2018**, *8*, 35–42. [[CrossRef](#)]
2. Li, J.; Xi, Z.; Pan, Y.T.; Spendelow, J.S.; Duchesne, P.N.; Su, D.; Li, Q.; Yu, C.; Yin, Z.; Shen, B.; et al. Fe Stabilization by Intermetallic L10-FePt and Pt Catalysis Enhancement in L10-FePt/Pt Nanoparticles for Efficient Oxygen Reduction Reaction in Fuel Cells. *J. Am. Chem. Soc.* **2018**, *140*, 2926–2932. [[CrossRef](#)] [[PubMed](#)]
3. Li, C.; Iqbal, M.; Lin, J.; Luo, X.; Jiang, B.; Malgras, V.; Wu, K.C.W.; Kim, J.; Yamauchi, Y. Electrochemical Deposition: An Advanced Approach for Templated Synthesis of Nanoporous Metal Architectures. *Acc. Chem. Res.* **2018**, *511*, 764–1773. [[CrossRef](#)] [[PubMed](#)]
4. Asset, T.; Job, N.; Busby, Y.; Crisci, A.; Martin, V.; Stergiopoulos, V.; Bonnaud, C.; Serov, A.; Atanassov, P.; Chattot, R.; et al. Porous Hollow PtNi/C Electrocatalysts: Carbon Support Considerations to Meet Performance and Stability Requirements. *ACS Catal.* **2018**, *8*, 893–903. [[CrossRef](#)]

5. Li, C.L.; Tan, H.B.; Lin, J.J.; Luo, X.L.; Wang, S.P.; You, J.; Kang, Y.H.; Bando, Y.; Yamauchi, Y.; Kim, J. Emerging Pt-based electrocatalysts with highly open nanoarchitectures for boosting oxygen reduction reaction. *Nano Today* **2018**, *21*, 91–105. [[CrossRef](#)]
6. Wang, X.; Choi, S.; Roling, L.T.; Luo, M.; Ma, C.; Zhang, L.; Chi, M.; Liu, J.; Xie, Z.; Herron, J.A.; et al. Palladium-platinum core-shell icosahedra with substantially enhanced activity and durability towards oxygen reduction. *Nat. Commun.* **2015**, *6*, 7594. [[CrossRef](#)] [[PubMed](#)]
7. Xie, S.; Choi, S.; Lu, N.; Roling, L.T.; Herron, J.A.; Zhang, L.; Park, J.; Wang, J.; Kim, M.J.; Xie, Z.; et al. Atomic Layer-by-Layer Deposition of Pt on Pd Nanocubes for Catalysts with Enhanced Activity and Durability toward Oxygen Reduction. *Nano Lett.* **2014**, *14*, 3570–3576. [[CrossRef](#)] [[PubMed](#)]
8. Lim, B.; Jiang, M.; Camargo, P.H.C.; Cho, E.C.; Tao, J.; Lu, X.; Zhu, Y.; Xia, Y. Pd-Pt Bimetallic Nanodendrites with High Activity for Oxygen Reduction. *Science* **2009**, *324*, 1302–1305. [[CrossRef](#)]
9. Lee, Y.W.; Ko, A.R.; Kim, D.Y.; Han, S.B.; Park, K.W. Octahedral Pt-Pd alloy catalysts with enhanced oxygen reduction activity and stability in proton exchange membrane fuel cells. *RSC Adv.* **2012**, *2*, 1119–1125. [[CrossRef](#)]
10. He, W.; Chen, M.; Zou, Z.; Li, Z.; Zhang, X.; Jin, S.A.; You, D.J.; Pak, C.; Yang, H. Oxygen reduction on Pd₃Pt₁ bimetallic nanoparticles highly loaded on different carbon supports. *Appl. Catal. B Environ.* **2010**, *97*, 347–353. [[CrossRef](#)]
11. Tang, Y.; Gao, F.; Yu, S.; Li, Z.; Zhao, Y. Surfactant-free synthesis of highly methanol-tolerant, polyhedral Pd-Pt nanocrystallines for oxygen reduction reaction. *J. Power Sources* **2013**, *239*, 374–381. [[CrossRef](#)]
12. Mazumder, V.; Chi, M.; More, K.L.; Sun, S. Core/Shell Pd/FePt Nanoparticles as an Active and Durable Catalyst for the Oxygen Reduction Reaction. *J. Am. Chem. Soc.* **2010**, *132*, 7848–7849. [[CrossRef](#)] [[PubMed](#)]
13. Vollmer, C.; Janiak, C. Naked metal nanoparticles from metal carbonyls in ionic liquids: Easy synthesis and stabilization. *Coord. Chem. Rev.* **2011**, *255*, 2039–2057. [[CrossRef](#)]
14. Liu, Y.; Chi, M.; Mazumder, V.; More, K.L.; Soled, S.; Henao, J.D.; Sun, S. Composition-Controlled Synthesis of Bimetallic PdPt Nanoparticles and Their Electro-oxidation of Methanol. *Chem. Mater.* **2011**, *23*, 4199–4203. [[CrossRef](#)]
15. Xia, Y.; Xiong, Y.; Lim, B.; Skrabalak, S.E. Shape-Controlled Synthesis of Metal Nanocrystals: Simple Chemistry Meets Complex Physics? *Angew. Chem. Int. Ed.* **2009**, *48*, 60–103. [[CrossRef](#)] [[PubMed](#)]
16. Mazumder, V.; Lee, Y.; Sun, S. Recent Development of Active Nanoparticle Catalysts for Fuel Cell Reactions. *Adv. Funct. Mater.* **2010**, *20*, 1224–1231. [[CrossRef](#)]
17. Antolini, E. Palladium in fuel cell catalysis. *Energy Environ. Sci.* **2009**, *2*, 915–931. [[CrossRef](#)]
18. Lim, B.; Jiang, M.; Yu, T.; Camargo, P.H.C.; Xia, Y. Nucleation and Growth Mechanisms for Pd-Pt Bimetallic Nanodendrites and Their Electrocatalytic Properties. *Nano Res.* **2010**, *3*, 69–80. [[CrossRef](#)]
19. Lim, B.; Jiang, M.; Tao, J.; Camargo, P.H.C.; Zhu, Y.; Xia, Y. Shape-Controlled Synthesis of Pd Nanocrystals in Aqueous Solutions. *Adv. Funct. Mater.* **2009**, *19*, 189–200. [[CrossRef](#)]
20. Yuan, Q.; Zhuang, J.; Wang, X. Single-phase aqueous approach toward Pd sub-10 nm nanocubes and Pd-Pt heterostructured ultrathin nanowires. *Chem. Commun.* **2009**, *43*, 6613–6615. [[CrossRef](#)]
21. Nguyen, V.L.; Ohtaki, M.; Matsubara, T.; Cao, M.T.; Nogami, M. New Experimental Evidences of Pt-Pd Bimetallic Nanoparticles with Core-shell Configuration and Highly Fine-Ordered Nanostructures by High-Resolution Electron Transmission Microscopy. *J. Phys. Chem. C* **2012**, *116*, 12265–12274. [[CrossRef](#)]
22. Wang, Y.; Ren, J.; Deng, K.; Gui, L.; Tang, Y. Preparation of Tractable Platinum, Rhodium, and Ruthenium Nanoclusters with Small Particle Size in Organic Media. *Chem. Mater.* **2000**, *12*, 1622–1627. [[CrossRef](#)]
23. Wei, T.; Fan, Z.; Luo, G.; Zheng, C.; Xie, D. A rapid and efficient method to prepare exfoliated graphite by microwave irradiation. *Carbon* **2009**, *47*, 337–339. [[CrossRef](#)]
24. Marcano, D.C.; Kosynkin, D.V.; Berlin, J.M.; Sinitskii, A.; Sun, Z.; Slesarev, A.; Alemany, L.B.; Lu, W.; Tour, J.M. Improved Synthesis of Graphene Oxide. *ACS Nano* **2010**, *4*, 4806–4814. [[CrossRef](#)] [[PubMed](#)]
25. Krishnamoorthy, K.; Veerapandian, M.; Yun, K.; Kim, S.J. The chemical and structural analysis of graphene oxide with different degrees of oxidation. *Carbon* **2013**, *53*, 38–49. [[CrossRef](#)]
26. Videla, A.H.M.; Ban, S.; Specchia, S.; Zhang, L.; Zhang, J. Non-noble Fe-N_x electrocatalysts supported on the reduced graphene oxide for oxygen reduction reaction. *Carbon* **2014**, *76*, 386–400. [[CrossRef](#)]
27. Ohma, A.; Shinohara, K.; Iiyama, A.; Yoshida, T.; Daimaru, A. Membrane and Catalyst Performance Targets for Automotive Fuel Cells by FCCJ Membrane, Catalyst, MEA WG. *ECS Trans.* **2011**, *41*, 775–784.

28. Qin, W.; Han, L.; Bi, H.; Jian, J.; Wu, X.; Gao, P. Hydrogen storage in a chemical bond stabilized Co₉S₈-graphene layered structure. *Nanoscale* **2015**, *7*, 20180–20187. [[CrossRef](#)]
29. Xing, R.; Wang, W.; Jiao, T.; Ma, K.; Zhang, Q.; Hong, W.; Qiu, H.; Zhou, J.; Zhang, L.; Peng, Q. Bioinspired polydopamine sheathed nanofibers containing carboxylate graphene oxide nanosheet for high-efficient dyes scavenger. *ACS Sustain. Chem. Eng.* **2017**, *5*, 4948–4956. [[CrossRef](#)]
30. Hummers, W.S.; Offeman, R.E. Preparation of Graphitic Oxide. *J. Am. Chem. Soc.* **1958**, *80*, 1339. [[CrossRef](#)]
31. Tang, Y.; Liu, Y.; Guo, W.; Chen, T.; Wang, H.; Yu, S.; Gao, F. Highly Oxidized Graphene Anchored Ni(OH)₂ Nanoflakes as Pseudocapacitor Materials for Ultrahigh Loading Electrode with High Areal Specific Capacitance. *J. Phys. Chem. C* **2014**, *118*, 24866–24876. [[CrossRef](#)]
32. Tang, Y.; Zhang, H.; Zhong, H.; Ma, Y. A facile synthesis of Pd/C cathode electrocatalyst for proton exchange membrane fuel cells. *Int. J. Hydrog. Energy* **2011**, *36*, 725–731. [[CrossRef](#)]
33. Tang, Y.; Zhang, H.; Zhong, H.; Xu, T.; Jin, H. Carbon-supported Pd-Pt cathode electrocatalysts for proton exchange membrane fuel cells. *J. Power Sources* **2011**, *196*, 3523–3529. [[CrossRef](#)]
34. Li, C.; Sato, R.; Kanehara, M.; Zeng, H.; Bando, Y.; Teranishi, T. Controllable Polyol Synthesis of Uniform Palladium Icosahedra: Effect of Twinned Structure on Deformation of Crystalline Lattices. *Angew. Chem. Int. Ed.* **2009**, *121*, 6883–6887. [[CrossRef](#)] [[PubMed](#)]
35. Marks, L.D. Experimental studies of small particle structures. *Rep. Prog. Phys.* **1994**, *57*, 603–649. [[CrossRef](#)]
36. Li, H.; Sun, G.; Li, N.; Sun, S.; Su, D.; Xin, Q. Design and Preparation of Highly Active Pt-Pd/C Catalyst for the Oxygen Reduction Reaction. *J. Phys. Chem. C* **2007**, *111*, 5605–5617. [[CrossRef](#)]
37. Czerwiński, A.; Grdeń, M.; Łukaszewski, M. Dual mechanism of hydrogen desorption from palladium alloys postulated on the basis of cyclic voltammetric studies. *J. Solid State Electrochem.* **2004**, *8*, 411–415. [[CrossRef](#)]
38. Duncan, H.; Lasia, A. Mechanism of hydrogen adsorption/absorption at thin Pd layers on Au (1 1 1). *Electrochim. Acta* **2007**, *52*, 6195–6205. [[CrossRef](#)]
39. Żurowski, A.; Grdeń, M.; Łukaszewski, M. Electrosorption of hydrogen into palladium-rhodium alloys. *Electrochim. Acta* **2006**, *51*, 3112–3117. [[CrossRef](#)]
40. Łukaszewski, M.; Kuśmierczyk, K.; Kotowski, J.; Siwek, H.; Czerwiński, A. Electrosorption of hydrogen into palladium-gold alloys. *J. Solid State Electrochem.* **2003**, *7*, 69–76. [[CrossRef](#)]
41. Grdeń, M.; Piaścik, A.; Koczorowski, Z.; Czerwiński, A. Hydrogen electrosorption in Pd-Pt alloys. *J. Electroanal. Chem.* **2002**, *532*, 35–42. [[CrossRef](#)]
42. Grdeń, M.; Łukaszewski, M.; Jerkiewicz, G.; Czerwiński, A. Electrochemical behaviour of palladium electrode: Oxidation, electrodisolution and ionic adsorption. *Electrochim. Acta* **2008**, *53*, 7583–7598. [[CrossRef](#)]
43. Savadogo, O.; Lee, K.; Oishi, K.; Mitsushima, S.; Kamiya, N.; Ota, K.I. New palladium alloys catalyst for the oxygen reduction reaction in an acid medium. *Electrochem. Commun.* **2004**, *6*, 105–109. [[CrossRef](#)]

